



Full-length visualisation of liquid oxygen disintegration in a single injector sub-scale rocket combustor

Dmitry I. Suslov*, Justin S. Hardi, Michael Oschwald

Institute of Space Propulsion, German Aerospace Center (DLR), Langer Grund, 74239 Hardthausen, Germany

ARTICLE INFO

Article history:

Received 27 July 2018

Received in revised form 22 November 2018

Accepted 23 December 2018

Available online 11 January 2019

Keywords:

Co-axial injector

Rocket combustion chamber

Combustion visualisation

ABSTRACT

This work presents results of an effort to create an extended experimental database for the validation of numerical tools for high pressure oxygen-hydrogen rocket combustion. A sub-scale thrust chamber has been operated at nine load points covering both sub- and supercritical chamber pressures with respect to the thermodynamic critical pressure of oxygen. Liquid oxygen and gaseous hydrogen were injected through a single, shear coaxial injector element at temperatures of around 120 K and 130 K, respectively. High-speed optical diagnostics were implemented to visualise the flow field along the full length of the combustion chamber. This work presents the analysis of shadowgraph imaging for characterising the disintegration of the liquid oxygen jet. The large imaging data sets are reduced to polynomial profiles of shadowgraph intensity which are intended to provide a more direct means of comparison with similarly reduced numerical results. Comparing half-lengths of these profiles across operating conditions show clear groupings of load points by combustion chamber pressure and mixture ratio. All load points appear to collapse to an inverse dependence of length on impulse flux ratio.

© 2019 The Authors. Published by Elsevier Masson SAS. This is an open access article under the CC BY-NC-ND license (<http://creativecommons.org/licenses/by-nc-nd/4.0/>).

1. Introduction

In the development of modern liquid rocket engines (LREs), injector head design is of the utmost importance for performance and combustion stability. Optimised designs must show high combustion efficiency in combination with low pressure drop across the injector at minimum chamber length and low manufacturing costs.

Modern LREs operated with liquid oxygen and hydrogen (LOX/H₂) like the Vulcain 2.1, Vinci, RS-25, J-2, LE-9, LE-5, and RD-0146 are equipped with classical shear-coaxial injector elements. While LOX is fed through the central tube at about 20–30 m/s, H₂ is delivered through a circumferential passage at high velocities of about 200–300 m/s. The LOX jet disintegration and mixing processes are driven by shear forces. Coaxial injectors provide adequate mixing characteristics, sufficient overall performance, and generally stable operation.

Today, the development of new rocket propulsion technology occurs during an era of increased competition and pressure to reduce development costs. However, the capabilities of computational systems are growing rapidly. Consequently, the main focus

in the development of new concepts, or upgrades to previous designs, has been shifting from the paradigm of the 1950s–1960s of verification through full-scale, hot-fire testing to numerical modelling and simulation.

Numerically oriented research activities of the last few years on LOX/H₂ propellants have improved understanding of the thermo- and fluid dynamic effects in highly turbulent, reactive flow fields at elevated pressures prevalent in LREs [1–7]. However, such works also highlight the continuing need for more experimental data suitable for validating models of injection and combustion at these conditions. Thorough validation of numerical models requires not only experimentally determined global parameters such as combustion chamber pressure and injection mass flow rates, but also precise information concerning the boundary conditions during the test.

Windowed combustion chambers with a single coaxial injector have been used for injection and combustion studies at representative conditions. Optical access has provided a wealth of information on injection and flame characteristics, as well as imaging of spray and flame topology valuable for validation of numerical models.

One such experiment with optical access is the combustor model ‘C’, abbreviated as BKC, operated at DLR Lampoldshausen. BKC was previously used to image LOX/H₂ and LOX/methane combustion to study flame anchoring [8–12]. Recently, it has been

* Corresponding author.

E-mail addresses: dmitry.suslov@dlr.de (D.I. Suslov), justin.hardi@dlr.de (J.S. Hardi), michael.oschwald@dlr.de (M. Oschwald).

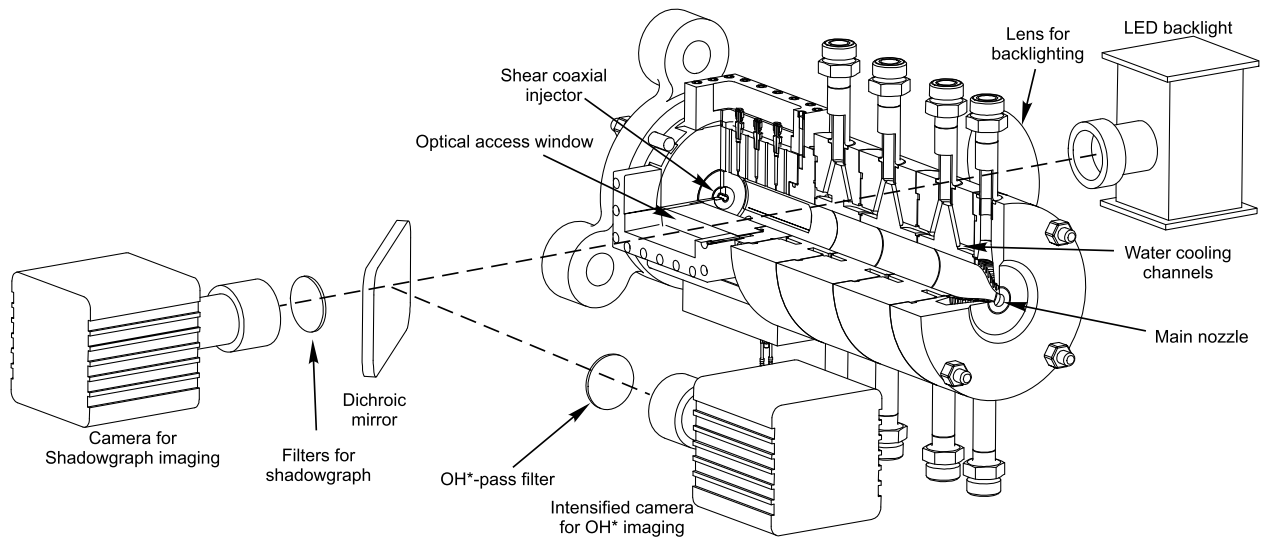


Fig. 1. Sketch of combustor model 'C' (BKC) including the optical setup.

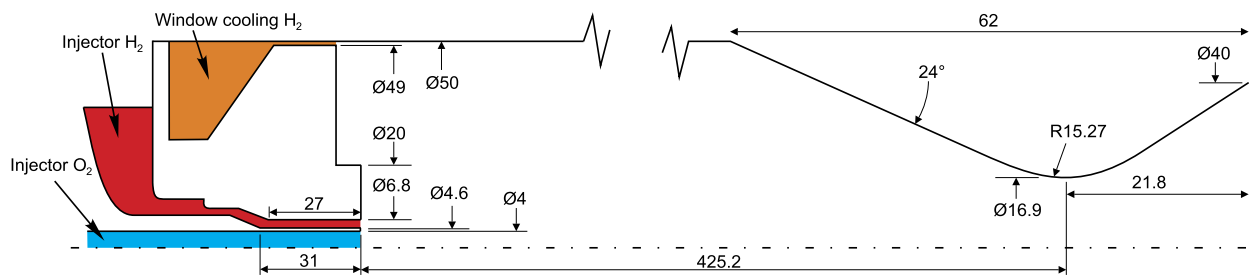


Fig. 2. BKC internal geometry. Horizontal dimensions are not drawn to scale.

used to produce a broad data set which is intended to provide a comprehensive quantitative and qualitative basis for validation of numerical models and contribute to the understanding of high pressure, LOX/H₂ combustion. Extensive measurements of the pressure and wall temperature distribution along the chamber were made to help define the boundary conditions in CFD models [13].

While in the earlier studies with BKC the optical imaging was limited to the near-injector region at the head end of the combustion chamber [8–12], here the flame has been imaged along the full length of the combustion chamber. This allows the topology and behaviour of the flame in its entirety to be studied. In the initial release of this data, Suslov et al. [13] presented measurements of the mean intact length of the LOX jet from high-speed shadowgraph imaging. Very few examples of such measurements from chambers with full-length optical access can be found in open literature [14].

This article presents analysis of the shadowgraph imaging captured for a range of operating conditions spanning sub- and supercritical pressures for oxygen. Imaging series are processed to extract information on the penetration length of the dense LOX jet and its rate of disintegration and consumption along the chamber axis. A method to reduce large imaging data sets to polynomial profiles is described. The resulting profiles are intended to provide a more direct method of comparison with similarly reduced numerical results. Finally, the dependence of jet length as observed from the profiles is found to have the strongest dependence on impulse flux ratio.

2. Experimental method

2.1. Combustor

The hot-fire tests presented here were carried out at the European Research and Technology Test Facility P8 at the German Aerospace Center (DLR), Lampoldshausen site [15]. This test facility enables investigations with the cryogenic propellants hydrogen, oxygen and natural gas at typical rocket engine operating conditions.

The experimental combustor, BKC, was specifically developed for intra-chamber injection and combustion studies by providing optical access for the application of visualisation and spectroscopic diagnostic techniques. It is highly versatile with interchangeable nozzles and injector head configurations. A sketch of the assembled BKC is shown in Fig. 1 and the internal geometry of the injector and combustion chamber are given in Fig. 2.

The inner diameter of the combustion chamber is 50 mm and the contraction ratio is 8.35. As can be seen in Fig. 2, the LOX post has no recess or taper, and the injector outlet stands proud of the faceplate by 3 mm. A circumferential film of H₂ with ambient temperature is injected along the walls to protect the optical access windows from the flame. This is labelled 'window cooling H₂' in Fig. 2. A cross-sectional view of the chamber at the position of the optical access window in Fig. 3 shows the interruption in the curvature of the chamber wall caused by the flat surface of the windows.

Pressure measurement is accomplished using pressure transducers with an accuracy of 1.2 to 3 bar. Temperature information is delivered by thermocouples with ± 2 K accuracy. These uncer-

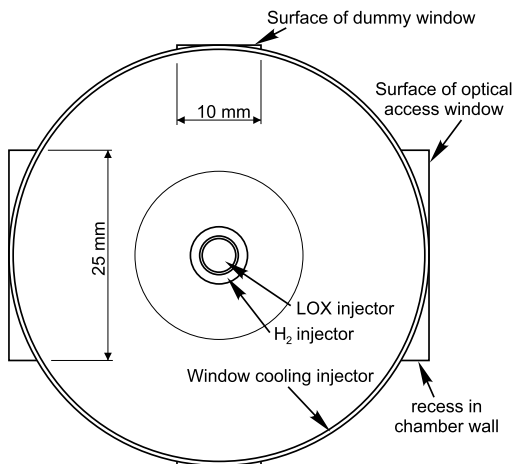


Fig. 3. Cross-section of the combustion chamber at the position of the optical access windows.

tainties are for the complete measurement chain. Flow rates are measured with a turbine flow meter for LOX and an orifice for H_2 , both with maximum errors of 3%. Fluid thermodynamic properties are estimated from the NIST database.

The combustion chamber is segmented into four separate, water-cooled sections and a nozzle. The windowed section contains quartz windows providing a viewing area 100 mm long and 25 mm high. By swapping the assembly order of these sections, the windowed section can be placed at various axial locations. This feature has been used to achieve optical access along nearly the full combustion chamber length, up to 370 mm of the 385-mm length. This distance is close to the length of real rocket engines

up to the nozzle throat. Fig. 4 illustrates the window positions and extent of the optical access.

2.2. Optical diagnostics

Fig. 1 also contains a sketch of the optical setup used in the experiments, shown here for the upstream window position. A photograph of the setup in the test cell of the P8 test facility is provided in Fig. 5. The setup was implemented to capture simultaneous shadowgraph imaging and filtered OH^* radiation imaging using high-speed cameras.

The system used for shadowgraph imaging used a continuous, LED back-lighting source with a wavelength of 528 nm. Before reaching the window on one side of the combustion chamber, the light was made parallel with a small aperture followed by an achromatic lens with a focal length of 1250 mm. On the other side of the chamber, imaging was made via a combination of yellow (GG495) and blue (BG38) filters, a 300 mm camera lens, and a field aperture to reduce scattered light from the surroundings. A Photron Fastcam SA5 recorded the images at 20,000 fps.

Achieved image resolution was around 140 $\mu\text{m}/\text{pixel}$. Camera exposure time was around 10 μs , depending on the chamber configuration. With LOX injection speeds of around 16 to 28 m/s, the exposure time results in a snapshot of the flow field which may have image smear of up to 2 pixels in some places. This is very little and is not expected to influence the analysis in this work.

OH^* radiation imaging was carried out simultaneously. To achieve the same field of view as for the shadowgraph imaging, a dichroic mirror was mounted in the optical path between the shadowgraph camera and combustion chamber window in a 45° orientation. Reflected UV light from the mirror passed through an OH^* filter (310 nm) and image intensifier before being recorded by

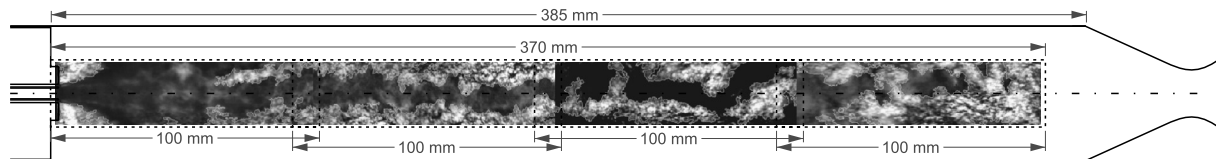


Fig. 4. Sketch of the combustion chamber and area of optical access, overlaid with example instantaneous shadowgraph images from load point 1 (60-bar chamber pressure).

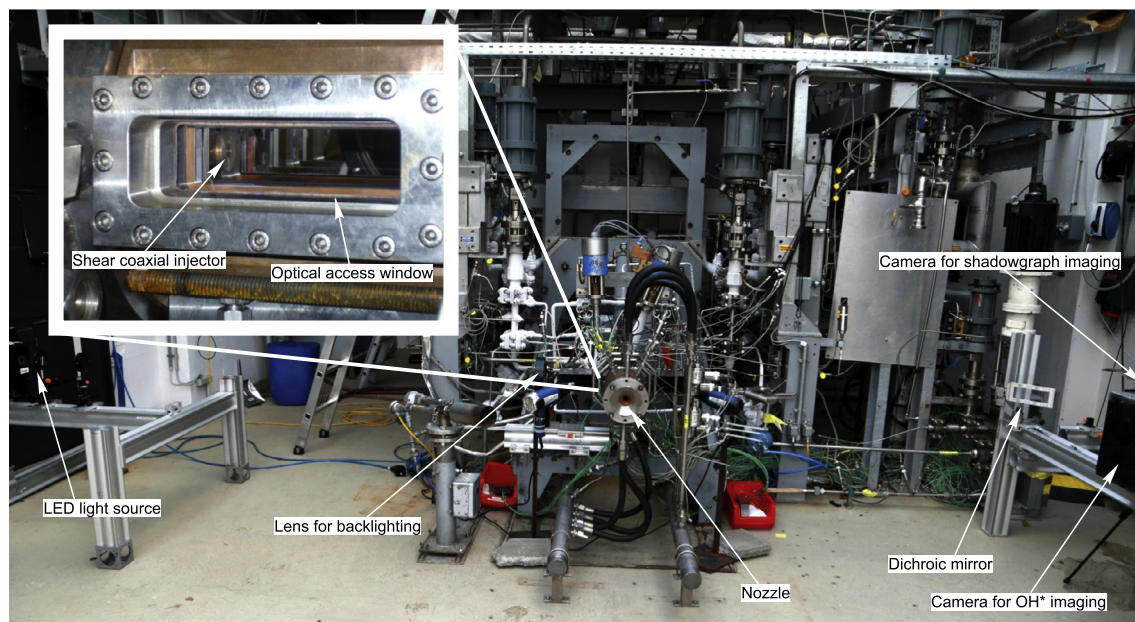


Fig. 5. Photograph of BKC and the optical setup in the test cell of the P8 test facility.

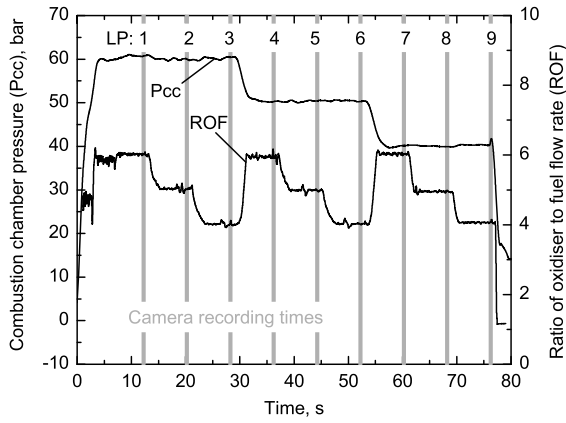


Fig. 6. Test sequence.

a second high-speed camera. Analysis of the OH* imaging is not presented in this article.

2.3. Test sequence

A well-established operating sequence was used to provide steady state conditions at three relevant pressure levels spanning sub- (40 bar), near- (50 bar), and supercritical (60 bar) conditions with respect to the critical pressure of oxygen. Each pressure level includes three steps of the ratio of oxidiser to fuel mass flow rate at the injector (ROF_{inj}), with values of 6, 5, and 4. In this way, nine operating conditions, or 'load points' (LPs), are achieved in each test run, as can be seen in Fig. 6.

The duration of each load step is 8 s, which allows a stable, steady-state thermal and flow condition to be reached. The last 0.5 s of each load point has been used for high speed optical imaging. These camera recording times are indicated by the grey bars in Fig. 6. After completing a test run, the window position is changed and the test sequence is repeated. The high precision regulation system and extensive experience of the test bench personnel provided repeatability of the test conditions to within $\pm 2\%$, which is important for the comparison of test runs with different window positions.

The injection conditions for all LPs are given in Table 1. These are mean values from the same time the camera was recording during each LP, and also averaged between tests with different window positions. It should be noted that the total, or 'bulk' value of ROF in the combustion chamber (ROF_{CC}) is significantly lower

than ROF_{inj} due to the contribution of the window cooling H_2 mass flow rate (\dot{m}_{WC}). The LOX and H_2 injection temperatures have been held relatively constant at 120 K and 160 K, respectively. LOX injection velocities of about 15–30 m/s and hydrogen velocities of about 350–440 m/s were of the same order of magnitude as those in comparable shear coaxial injector studies [8,14]. The calculation of the injection velocities is based on the full injection area without consideration of the boundary layer displacement thickness.

The final column of Table 1 contains estimates of the experimental uncertainty in the parameters for all load points. It includes both absolute measurement error and the variance between the measured values from the four tests performed to gather imaging from each of the four combustor configurations. The maximum sensor error and variance values are taken for each parameter, so the values of uncertainty are considered to be conservative.

3. Composite images

With sets of high-speed imaging from all LPs and all window positions, composite images of the full chamber length for each operating condition were produced. Example instantaneous shadowgraph images from LP1 (60 bar, ROF 6) are overlaid in Fig. 4 to assist in interpreting the extent of optical access. A further example of a raw, composite image is give for LP9 at the top of Fig. 7. In both examples the dense LOX jet can be discerned extending along a meandering path from the injection plane until it is consumed by combustion.

However, resolving the LOX core is hindered by the busy background in the image. Rather than a blank (white) image of the backlight, the background surrounding the LOX structures has a grainy texture due to strong, fine-scaled density gradients in the turbulent, reacting combustion gases. The high variation in optical absorption coefficient and refractive index cannot be washed out by the backlighting intensity at these operating conditions.

To improve comparability of images between window positions and LPs, the shadowgraph images have been converted to the binary (black and white) images. The conversion uses texture-based filtering rather than thresholding. Edge detection with the Sobel operator is combined with several morphological operations to identify and merge strong, small-scale contrast gradients. This approach removes the grainy textured background while preserving the larger areas corresponding to dense oxygen structures, as can be seen in the example binarised composite image in the middle of Fig. 7. Some artefactual inclusions remain, mostly near the edges

Table 1
Operating conditions.

Load point		1	2	3	4	5	6	7	8	9	Max. uncertainty ^b
Pcc	bar	62.1	60.9	60.9	50.8	50.7	50.5	40.4	40.0	40.4	± 2.2 bar
ROF_{inj}^a	–	5.9	4.9	4.0	5.9	4.9	4.0	6.0	4.9	4.0	$\pm 8.2\%$
ROF_{CC}^a	–	1.3	1.2	1.1	1.3	1.2	1.1	1.3	1.2	1.1	$\pm 8.8\%$
\dot{m}_{O_2}	g/s	356	329	311	275	265	253	214	206	200	$\pm 5.2\%$
\dot{m}_{H_2}	g/s	60	67	78	47	54	64	36	42	50	$\pm 3.7\%$
\dot{m}_{WC}	g/s	209	203	199	164	162	160	127	127	127	$\pm 4.8\%$
P_{O_2}	bar	103.8	96.1	92.6	76.1	74.1	72.2	56.6	55.1	54.7	± 4.3 bar
P_{H_2}	bar	69.1	69.8	73.7	56.2	57.8	60.6	44.4	45.6	48.2	± 4.9 bar
P_{WC}	bar	64.0	62.9	62.8	52.4	52.2	52.0	41.5	41.2	41.5	± 3.3 bar
T_{O_2}	K	114	114	114	114	114	115	116	118	118	± 4.4 K
T_{H_2}	K	154	155	158	159	159	159	161	160	159	± 9.9 K
T_{WC}	K	294	299	302	304	303	303	302	302	301	± 9.3 K
$u_{O_2}^a$	m/s	27	25	24	21	21	20	17	16	16	$\pm 5.7\%$
$u_{H_2}^a$	m/s	325	371	444	318	367	434	309	361	422	$\pm 7.8\%$
u_{WC}^a	m/s	269	271	269	265	262	259	256	258	255	$\pm 5.2\%$
VR^a	–	11.9	14.7	18.5	15.0	17.9	22.0	18.3	22.2	26.5	
J^a	–	1.3	1.9	3.0	1.6	2.3	3.5	2.0	2.9	4.2	

^a Calculated parameter.

^b Combined maximum measurement error and variance between tests.

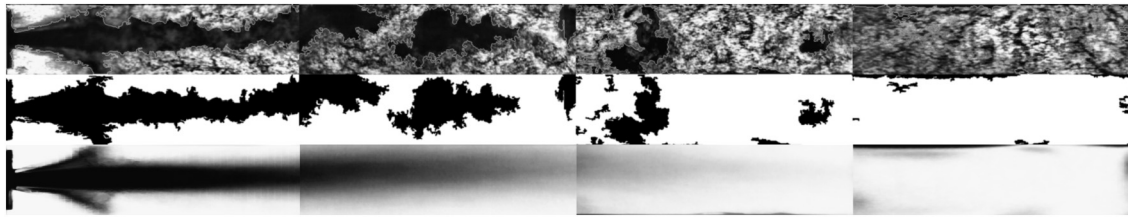


Fig. 7. Example of an instantaneous, full-length composite, raw shadowgraph image for LP9, and the corresponding binarised version for dense LOX detection (top and middle). Below is the averaged intensity distribution from 500 binarised images.

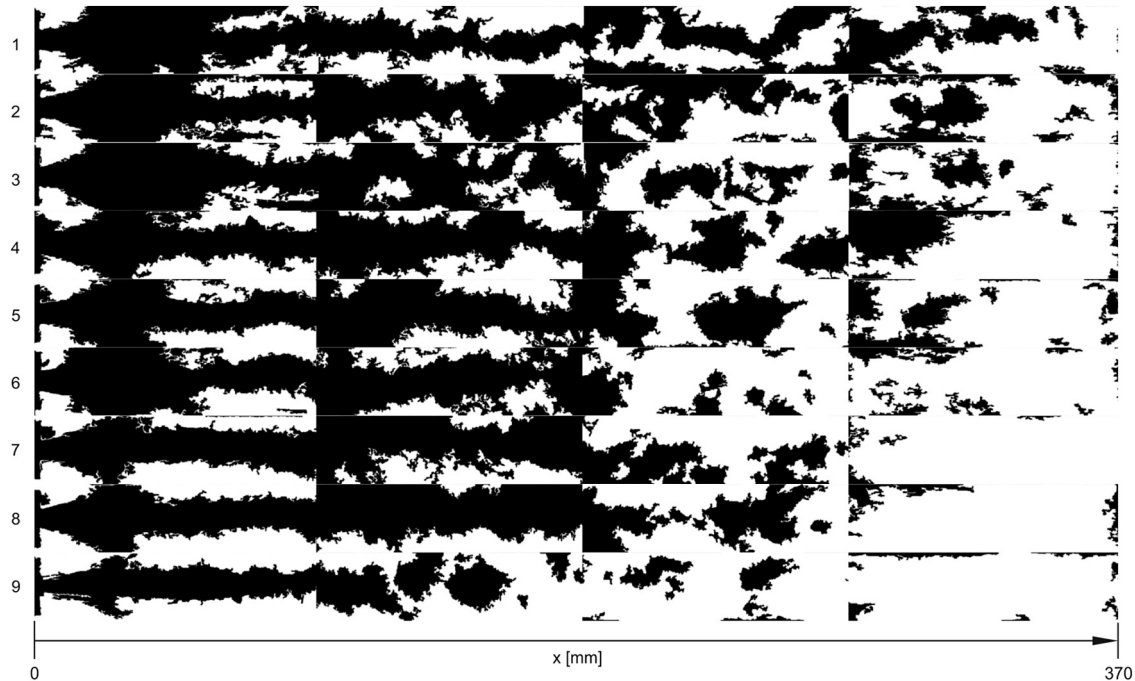


Fig. 8. Full-length composite, binarised images for all nine load points.

of the two downstream windows from consistent attenuation of backlighting. In general, the method isolates coherent structures of LOX from the turbulent background well, and minimises the influence from optical effects.

Time-averaged images can also be produced after binary conversion, for example at the bottom of Fig. 7. These give a better indication of the mean location of dense oxygen than time-averaged raw images, in which the contribution from the LOX shadow is overwhelmed by the cumulative contribution from the high-contrast, turbulent background. The averaged imaging is analysed later in Section 4.

Binarised composite images for all LPs are compared in Fig. 8. A short distance downstream of injection, about $x = 20$ mm, the jet appears to spread all the way to the edges of the window and fill the viewing area for up to half the length of the first window position. This ‘shoulder’ of the flame is actually H_2 which becomes opaque as it expands following injection, obscuring the view of the LOX core. Further downstream the LOX core becomes easily recognised.

Thread-like structures can be seen to form from the surface of the core. Downstream, lumps of LOX break away from the end of the jet and are convected downstream as they continue to vapourise and be consumed by combustion. A general trend of decreasing extent of LOX presence can be seen from LP 1 to 9. At the 40-bar Pcc conditions (LPs 7–9) consumption of the LOX core is completed by $x = 280$ mm (end of third window position), while at the 60-bar conditions (LPs 1–3) several dark LOX spots are visible up to the end of the observation area. When viewing high-speed

images, these spots of LOX are observed to travel beyond the end of the window. It is not known whether they are consumed before reaching the nozzle.

4. Axial LOX profiles

The instantaneous binary images presented previously give a feel for the dynamic, turbulent nature of the LOX core break up and consumption processes. We now seek a way to characterise the progress of these processes with axial location in the chamber. The goal is to reduce the imaging data to a form more easily comparable with the results of numerical simulations.

Time-averaged composite images are used for this purpose, with a comparison of the full set of LPs presented in Fig. 9. Each image is the average of 500 binary images. This number was determined by studying the convergence of the image topology during averaging. Binary images were added sequentially to the averaged image, and after each addition the image gradient field was determined. The difference to the gradient field in the predecessor image is taken to represent the change in LOX topology. With increasing number of added binary images, this topology change parameter asymptotes towards zero. For the current data sets, the change was negligibly small after around 500 images. Including further images from the available data set simply degraded the contrast of the mean image. This number was thus found to produce the best quality of averaged image where the topology of the flow field was converged.

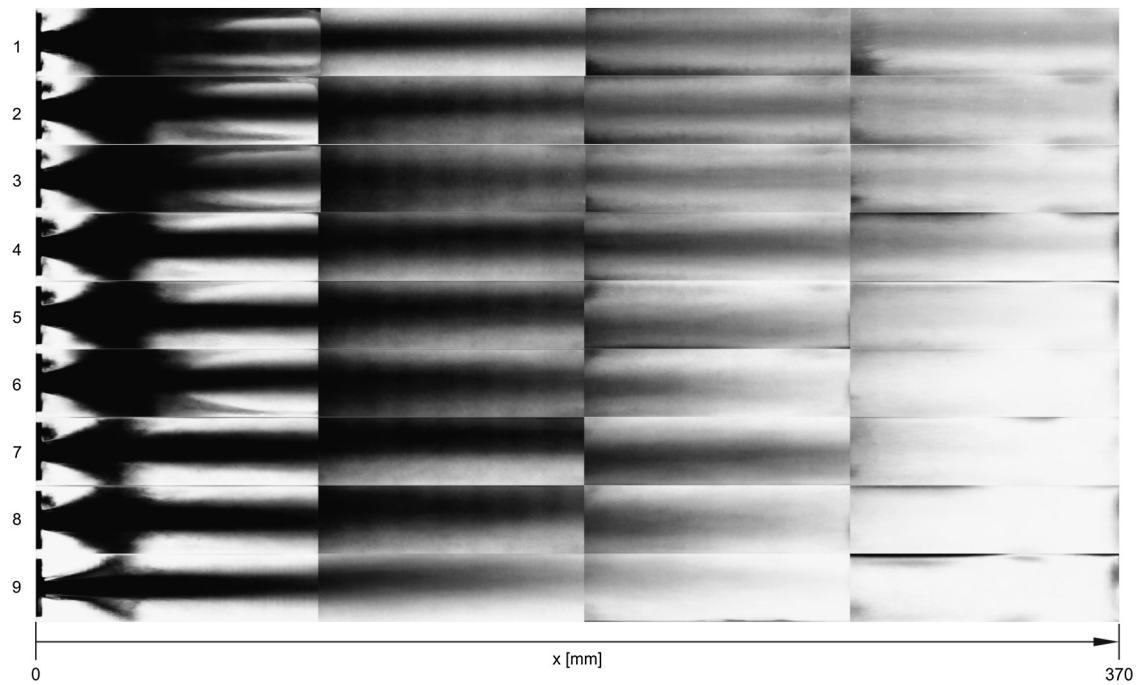


Fig. 9. Full-length composite, averaged intensity distributions for all nine load points.

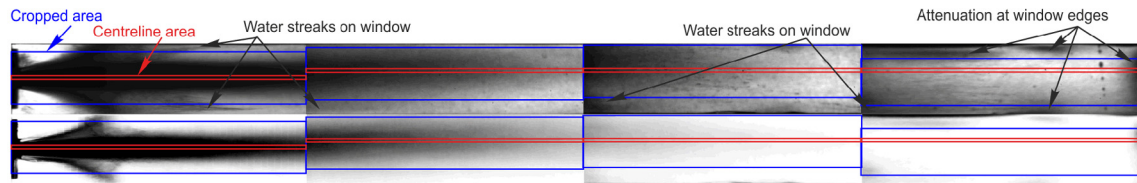


Fig. 10. Averaged raw (above) and averaged binary (below) images for LP9 indicating the sampling regions for mean 'cropped' and 'centreline' intensity profiles.

Axial profiles of mean intensity were produced from the composite images. Three different sampling areas were defined for this purpose. First, the entire height of the optically accessible area was taken. Second, a cropping window was used to exclude much of the non-LOX artefacts at the upper and lower edges of the images. The cropping windows are indicated by the blue boxes in Fig. 10 for LP9. Comparing with the averaged raw image (above) helps to identify and avoid artefactual dark regions in the averaged binary image (below). Some dark areas are caused by backlighting attenuation at the edges of windows, and some from streaks of water condensing on the window surface, indicated in Fig. 10. Third, a narrow area best coinciding with the path of the centreline of the LOX jet was defined for each window position, indicated in red in Fig. 10.

From these sampling regions, transversally averaged, axial intensity profiles were produced and are plotted for the example of LP9 in Fig. 11. A value of 1.0 means fully black, where the sample region was always filled with LOX. The profiles for whole-window, cropped, and centreline sample regions all show a gradual decrease in mean intensity with axial distance for each window position, but are discontinuous from one window to the next. This is mostly due to use of different camera or backlight settings when readjusting the optical setup between tests.

The resulting discontinuity in image contrast can be compensated by assuming continuity of LOX jet behaviour across window position limits. The profiles from the second, third, and fourth window positions are proportionally reduced such that the values in the leading 10 mm coincide with those of the preceding profile where they overlap. This adjustment is performed for the cropped (blue) and centreline (red) profiles in Fig. 12. The original, whole-

window profile is excluded from this point because the cropped profile can be seen to reduce the influence of edge effects in the imaging, particularly in the leading parts of the profiles where water streaks on the windows most affect the binary images.

From this point the objective is to fit a polynomial to the profile data for a clean basis of comparison between LPs and with numerical results. Further artefactual content present in the profiles is excluded as shown in Fig. 13. For the window profile (blue), only the last 20 mm from the first window position represent the contribution of LOX alone. The first 70 mm of the profile are influence by the flame shoulder (expanding H_2), and the last few millimetres (from around $x = 95$) increase sharply due to a dark strip at the end of the image caused by the chamfer on quartz window. These parts of the profile (light blue) are excluded from the subsequent polynomial fitting.

Polynomials were fit to each of the now cleaned sets of profile data with a least-squares optimisation, with the resulting polynomials for LP9 plotted in Fig. 14. The following constraints were applied in fitting a polynomial to the window profile data:

- A sixth order polynomial was found to best fit the cropped data sets from all LPs.
- The width of the LOX core at the injection plane is the same for all LPs. This could be determined from the trough in the profile at $x = 3$ mm for all LPs. The first point of the polynomial was therefore fixed at $x = 3$, $y = 0.22$ (22% intensity).
- The polynomial extends from $x = 3$ to the first minimum below 2% intensity, effectively the zero crossing, or to where it leaves the field of view ($x = 370$).

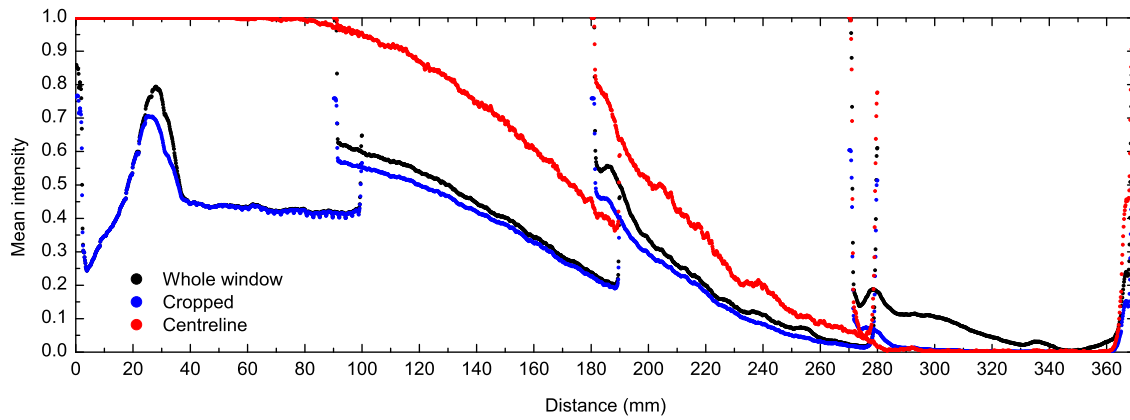


Fig. 11. Raw axial intensity profiles for LP9.

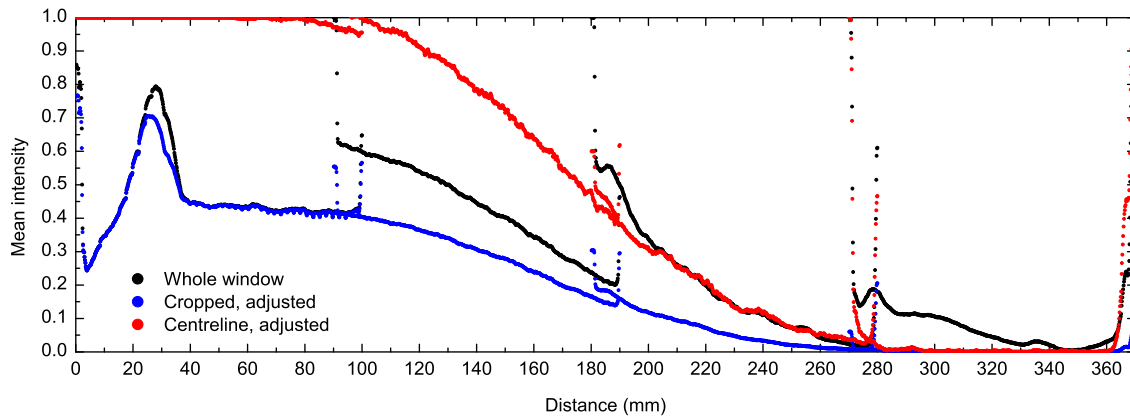


Fig. 12. Scaled axial intensity profiles for LP9.

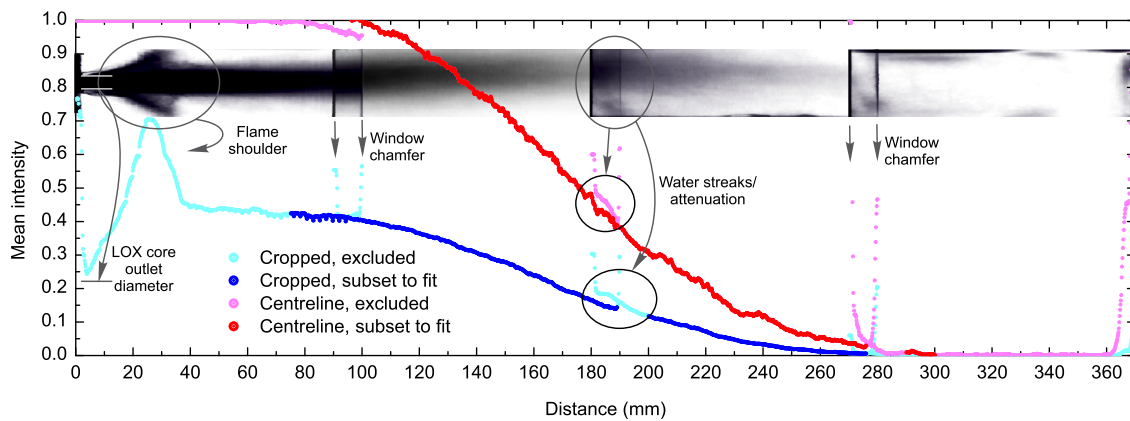


Fig. 13. Scaled and cropped axial intensity profiles for LP9.

The following constraints were applied in fitting to the centreline profile data:

- A fifth order polynomial was found to best fit the centreline data sets from all LPs.
- The polynomial fit begins at maximum intensity ($y = 1.0$) and at the axial location where the LOX core begins to breakup. This does not occur before $x = 100$ mm for any LP (although it appears to be the case in the LP9 example in Fig. 14, the slight reduction in intensity is caused by occasional artefactual detection of flame radiation in front of the LOX core). The starting point of the polynomial chosen as the x -location in the profile from the second window position where y drops below 0.99.

- The polynomial extends to the first minimum below 2% intensity, effectively the zero crossing, or to where it leaves the field of view ($x = 370$).

Four rocket combustor hot-fire tests and tens of thousands of shadowgraph images have been reduced to the two polynomials in Fig. 14. The physical interpretation and expected utility of these profiles will now be explained.

The window profile describes the axial distribution of the presented area of LOX in the flow. It begins with the value of the width of the injector and initially increases. This initial increase reflects an expansion of the jet which increases its presented area in the shadowgraph imaging. Then, the jet begins to breakup, with lumps shed from the end of the intact part of the LOX

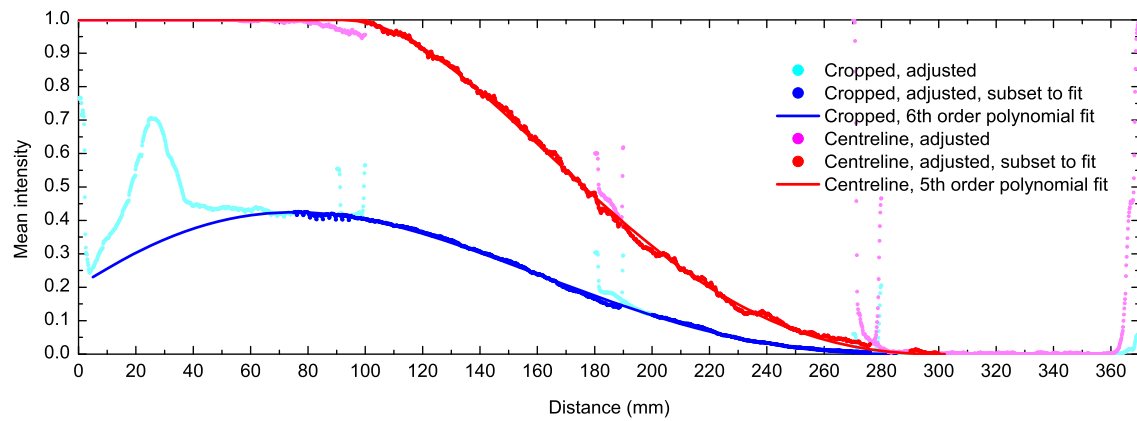


Fig. 14. Polynomial fitting of intensity profiles for LP9.

core which are accelerated away with the faster surrounding flow. This increasing gap causes the profile to decrease. The continuing decrease to zero reflects the further breakup and vaporisation of these shed lumps of LOX. This profile could potentially be compared to profiles of the projected area of oxygen density iso-surfaces from CFD simulations.

The centreline profile describes the axial probability density distribution of LOX presence at the core axis. It begins with a value of 1.0 (continuous LOX jet) and begins to decrease at the position where the first break points in the jet occur. The continuing decrease to zero reflects the further breakup and vaporisation of LOX along the centreline of the jet. This profile could potentially be compared to a numerically determined centreline profile of oxygen density. It is hoped to serve a similar utility as the density profiles measured from non-reacting nitrogen jets by Mayer et al. [16].

5. Results and discussion

The analysis presented here is based on the assumption that black areas in the binary images indicate the location of LOX (dense oxygen), where the backlighting was most effectively absorbed. This does not mean that white regions have an oxygen concentration of zero, just that the LOX has vaporised and is mixing and reacting with H_2 . Extending this assumption to the mean images, we take local intensity to be proportional to the local probability of dense LOX being present in the flow. The term 'dense' cannot be more precisely defined, since there is no known calibration of shadowgraph image intensity with local oxygen density. However, the results are anchored to intensity values where the presence of pure LOX in the image is known. In the case of the window profile this corresponds to the side area of the jet at the

injector exit, and in the centreline case it is the point where the intact LOX core first experiences a break point.

Fitted profiles for the different LPs can now be compared. Figs. 15 to 20 plot the fitted polynomials, first for the window (cropped image) and then the centreline LOX profiles, grouped by operating Pcc. The window profiles have been normalised to the intensity value corresponding to the LOX jet width at injection.

Fig. 15 shows the profiles for load points at 60-bar Pcc (LPs 1–3). The jet area expands to around 1.8 times its original width at injection at LP1, and over 2.0 times the original width at LP3. The expansion therefore increases with velocity ratio (VR) and impulse flux ratio (J) (see Table 1). However, this trend appears to be reversed for the 50- and 40-bar LPs in Figs. 16 and 17, respectively.

The intensities for LPs 1–3 in Fig. 15 are all non-zero at the end of the viewing area, meaning significant LOX structures departed the viewing area intact when the optical segment was next to the nozzle. The intensities here decrease in order of LP, perhaps in dependence with LOX mass flow rate. This trend in the extent of intensity at the end of the profiles is consistent with the other LPs shown in Figs. 16 and 17. It is also consistent in all groups of centreline profiles in Figs. 18 to 20.

A further observation consistent in both types of profiles is that the extent of LOX is greater at the ROF-6 LPs than the ROF-4 LPs of the preceding Pcc level. That is, LOX presence lasts longer at LP4 (50 bar, ROF 6) than at LP3 (60 bar, ROF 4), and longer at LP7 (40 bar, ROF 6) than at LP6 (50 bar, ROF 4). This observation is supported by visual comparison of the composite averaged images in Fig. 9. This apparent 'grouping' of LOX lengths by Pcc may reflect some dependence on ROF or H_2 injection velocity (u_{H_2}), VR, or J, since these are the parameters which do not decrease monotonically with increasing LP number.

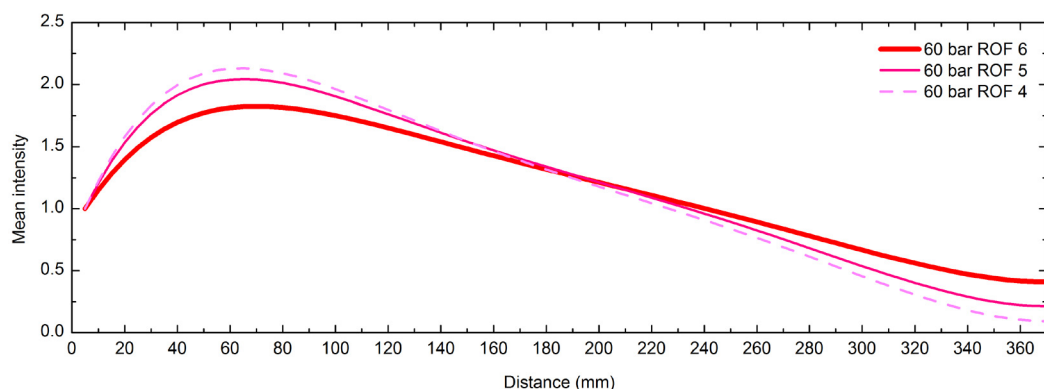


Fig. 15. Fitted window intensity profiles for 60-bar load points (LPs 1–3).

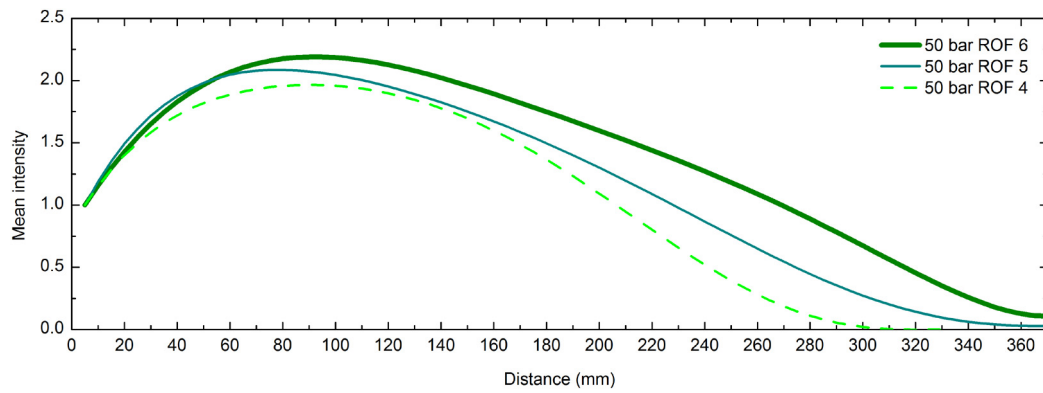


Fig. 16. Fitted window intensity profiles for 50-bar load points (LPs 4–6).

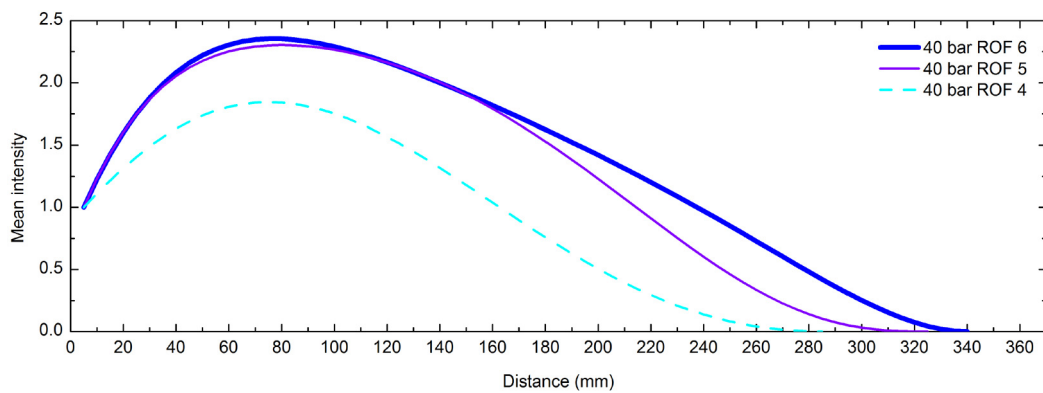


Fig. 17. Fitted window intensity profiles for 40-bar load points (LPs 7–9).

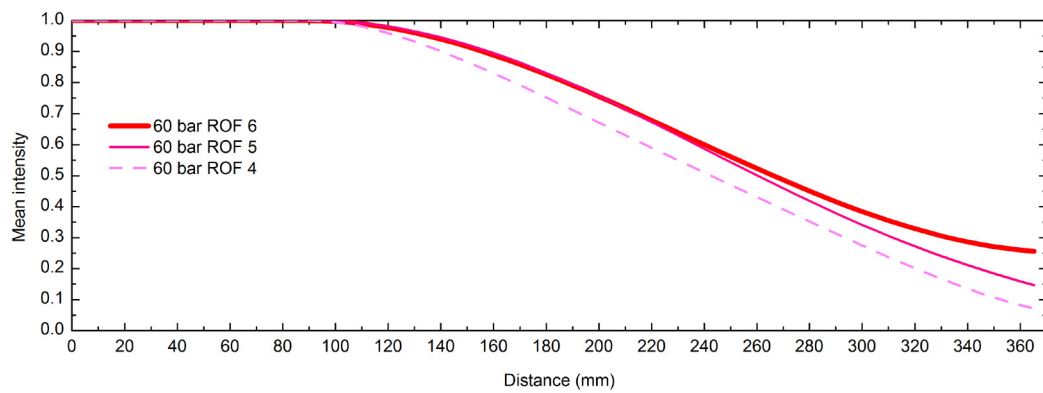


Fig. 18. Fitted centreline intensity profiles for 60-bar load points (LPs 1–3).

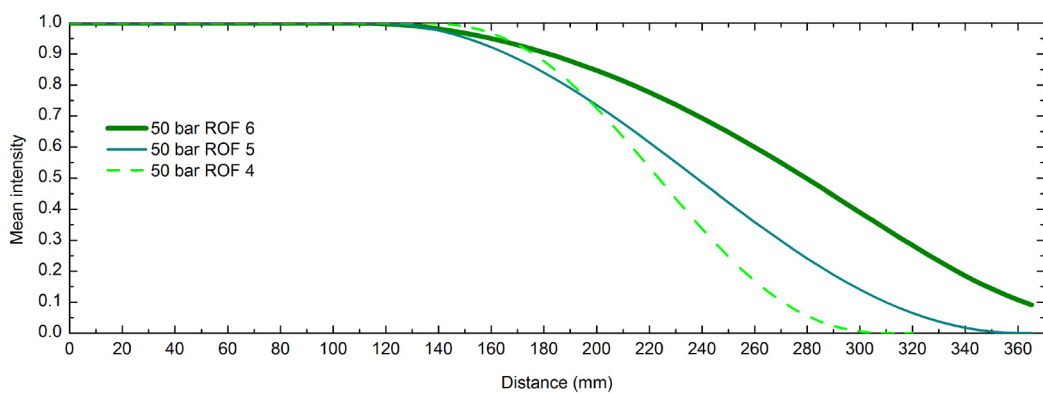


Fig. 19. Fitted centreline intensity profiles for 50-bar load points (LPs 4–6).

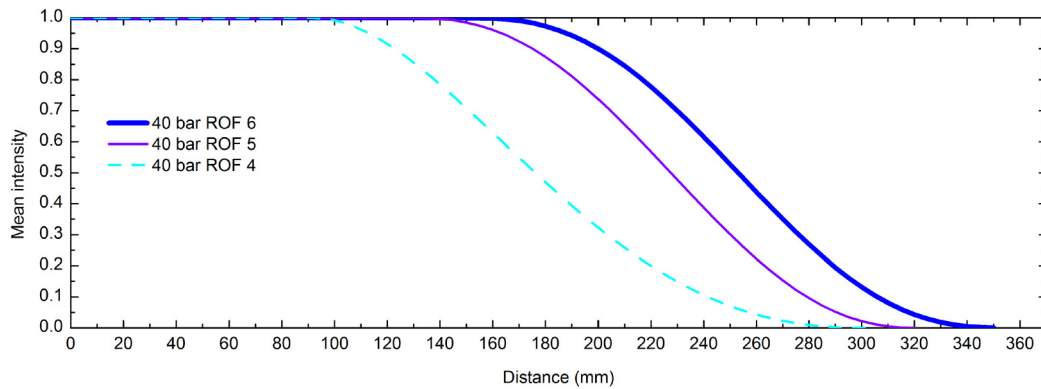


Fig. 20. Fitted centreline intensity profiles for 40-bar load points (LPs 7–9).

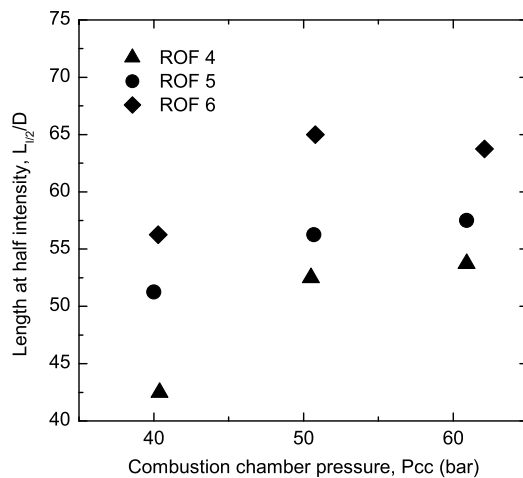


Fig. 21. Length at half intensity from the window profiles.

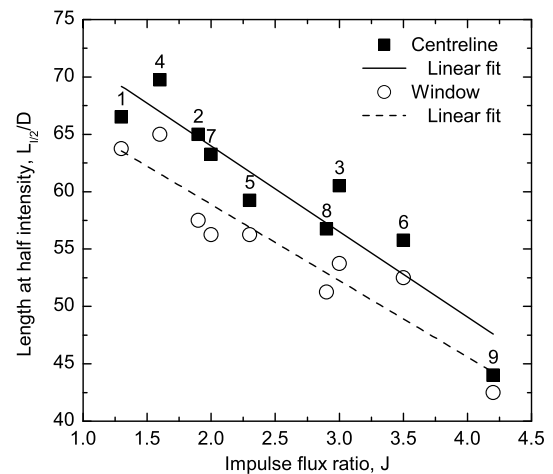


Fig. 22. Length at half intensity vs impulse flux ratio.

To check this, values of length at half intensity were compared for all LPs. The length at a value of half of the peak profile intensity is taken because the full length of some profiles extends beyond the observation window. Taking the half-intensity length allows all LPs to be compared at once. As can be seen in Fig. 21, with length values from the window profiles, and normalised by LOX injector diameter (D), there is clear grouping by P_{cc} and ROF. The values from all LPs collapse to an apparent inverse linear dependence on impulse flux ratio (J), as seen in Fig. 22. This supports the classically held view that J is the injection parameter with the greatest influence on jet disintegration length.

6. Conclusions

High-speed shadowgraph imaging was used to detect the extent of dense oxygen presence in the flow field of an experimental rocket combustor with a single injector. The geometry and injection conditions are representative of industrial engines using oxygen–hydrogen propellants with shear-coaxial injection elements. The experiment was operated at a range of conditions spanning sub- to supercritical pressures with respect to the critical pressure of oxygen, and thus cover important thermodynamic regimes for oxygen–hydrogen engines.

Large sets of shadowgraph images were binarised, time-averaged, and then reduced to transversally averaged, axial intensity distributions. These intensity distributions were approximated with polynomials which describe the axial probability density profile of detecting dense oxygen. The profiles are expected to be of use in comparing the experimental data with the results of numerical simulations for the purpose of model validation.

The value of these profiles is based on the assumption that the intensity in the mean images is proportional to the local probability of dense LOX being present in the flow. The intensity cannot be related more directly to a physical quantity such as density since calibration of shadowgraph image intensity with local oxygen density is lacking. However, the results are normalised to image intensity at locations where the presence of pure LOX is known.

Taking the measure of length at half intensity from the profiles, the LOX jet disintegration behaviour can be compared across load points. The defining load point conditions of chamber pressure and mixture ratio cause distinct groupings of jet length. The strongest dependency found was that of jet length on inverse momentum flux ratio (J number).

Conflict of interest statement

The authors are not aware of any conflict of interest.

Acknowledgements

The authors would like to thank the P8 test facility team and Bernhard Knapp for their indispensable contributions during the test campaign.

References

- [1] J.C. Oefelein, Mixing and combustion of cryogenic oxygen–hydrogen shear-coaxial jet flames at supercritical pressure, *Combust. Sci. Technol.* 178 (1–3) (2006) 229–252, <https://doi.org/10.1080/00102200500325322>, <http://www.tandfonline.com/doi/abs/10.1080/00102200500325322>.

- [2] T. Schmitt, L. Selle, B. Cuenot, T. Poinso, Large-eddy simulation of transcritical flows, *C. R. Méc.* 337 (6) (2009) 528–538, <https://doi.org/10.1016/j.crme.2009.06.022>, <http://www.sciencedirect.com/science/article/pii/S1631072109000941>.
- [3] M. Lempke, P. Gerlinger, M.J. Seidl, M. Aigner, Unsteady high-order simulation of a liquid oxygen/gaseous hydrogen rocket combustor, *J. Propuls. Power* 31 (6) (2015) 1715–1726.
- [4] A. Urbano, L. Selle, G. Staffelbach, B. Cuenot, T. Schmitt, S. Ducruix, S. Candel, Exploration of combustion instability triggering using large eddy simulation of a multiple injector liquid rocket engine, *Combust. Flame* 169 (2016) 129–140.
- [5] D.T. Banuti, V. Hannemann, K. Hannemann, B. Weigand, An efficient multi-fluid-mixing model for real gas reacting flows in liquid propellant rocket engines, *Combust. Flame* 168 (2016) 98–112.
- [6] D.T. Banuti, P.C. Ma, M. Ihme, Phase separation analysis in supercritical injection using large-eddy-simulation and vapor-liquid-equilibrium, in: 53rd AIAA/SAE/ASEE Joint Propulsion Conference, AIAA 2017-4764, 2017, <https://doi.org/10.2514/6.2017-4764>.
- [7] S.K. Beinke, D. Banuti, J.S. Hardi, M. Oschwald, B.B. Dally, Modelling of a coaxial LOX/GH2 injection element under high frequency acoustic disturbances, in: C. Bonnal, M. Calabro, S.M. Frolov, L. Calfetti, F. Maggi (Eds.), *Progress in Propulsion Physics*, vol. 11, EDP Sciences, 2018, <http://www.eucass-proceedings.eu>.
- [8] W. Mayer, B. Ivancic, A. Schik, U. Hornung, Propellant atomization and ignition phenomena in liquid oxygen/gaseous hydrogen rocket combustors, *J. Propuls. Power* 17 (4) (2001) 794–799, <http://data-ro/refbase/show.php?record=7698>.
- [9] B. Ivancic, W. Mayer, Time- and length scales of combustion in liquid rocket thrust chambers, *J. Propuls. Power* 18 (2) (2002) 247–253, <https://doi.org/10.2514/2.5963>, <http://arc.aiaa.org/doi/abs/10.2514/2.5963>.
- [10] J. Lux, D. Suslov, M. Bechle, M. Oschwald, O.J. Haidn, Investigation of sub- and supercritical lox/methane injection using optical diagnostics, in: 42nd AIAA/ASME/SAE/ASEE Joint Propulsion Conference & Exhibit, AIAA, Sacramento, California, 2006, pp. 1–11, <http://arc.aiaa.org/doi/abs/10.2514/6.2006-5077>.
- [11] J. Lux, O.J. Haidn, Effect of recess in high-pressure liquid oxygen/methane coaxial injection and combustion, *J. Propuls. Power* 25 (1) (2009) 24–32, <https://doi.org/10.2514/1.37308>, <http://arc.aiaa.org/doi/abs/10.2514/1.37308>.
- [12] J.J. Smith, G.M. Schneider, D. Suslov, M. Oschwald, O.J. Haidn, Steady-state high pressure LOX/H2 rocket engine combustion, *Aerosp. Sci. Technol.* 11 (1) (2007) 39–47, <https://doi.org/10.1016/j.ast.2006.08.007>, <http://linkinghub.elsevier.com/retrieve/pii/S1270963806001398>.
- [13] D.I. Suslov, J.S. Hardi, B. Knapp, M. Oschwald, Hot-fire testing of LOX/H2 single coaxial injector at high pressure conditions with optical diagnostics, in: C. Bonnal, M. Calabro, S.M. Frolov, L. Calfetti, F. Maggi (Eds.), *Progress in Propulsion Physics*, vol. 11, EDP Sciences, 2018, <http://www.eucass-proceedings.eu>.
- [14] J.M. Locke, S. Pal, R.D. Woodward, R.J. Santoro, High speed visualization of LOX/GH2 rocket injector flowfield: hot-fire and cold-flow experiments, in: 46th AIAA/ASME/SAE/ASEE Joint Propulsion Conference & Exhibit, AIAA, Nashville, Tennessee, July 2010, pp. 1–18.
- [15] A. Haberkretzl, D. Gundel, K. Bahlmann, J.L. Thomas, J. Kretschmer, P. Vuillermoz, European research and technology test bench P8 for high pressure liquid rocket propellants, in: 36th AIAA/ASME/ASEE Joint Propulsion Conference and Exhibit, AIAA, Huntsville, Alabama, 2000.
- [16] W. Mayer, J. Telaar, R. Branam, G. Schneider, J. Hussong, Raman measurements of cryogenic injection at supercritical pressure, *Heat Mass Transf.* 39 (2003) 709–719.